Quantum paramagnetism in the decorated square-kagome antiferromagnet $Na_6Cu_7BiO_4(PO_4)_4Cl_3$

Nils Niggemann,[1, 2, 3, *] Nikita Astrakhantsev,[4, *] Arnaud Ralko,[5, 3, *] Francesco Ferrari,[6, 3, *] Atanu Maity,[3] Tobias Müller,[7]

Johannes Richter,[8, 9] Ronny Thomale,[7, 3] Titus Neupert,[4] Johannes Reuther,[1, 2, 3] Yasir Iqbal,[3] and Harald O. Jeschke[10, 3]

[1]*Dahlem Center for Complex Quantum Systems and Fachbereich Physik, Freie Universität Berlin, 14195 Berlin, Germany*

[2]*Helmholtz-Zentrum Berlin für Materialien und Energie, Hahn-Meitner-Platz 1, 14109 Berlin, Germany*

[3]*Department of Physics and Quantum Centre of Excellence for Diamond and Emergent Materials (QuCenDiEM),*
Indian Institute of Technology Madras, Chennai 600036, India

[4]*Department of Physics, University of Zürich, Winterthurerstrasse 190, CH-8057 Zürich, Switzerland*

[5]*Institut Néel, UPR2940, Université Grenoble Alpes, CNRS, Grenoble, FR-38042 France*

[6]*Institut für Theoretische Physik, Goethe Universität Frankfurt,*
Max-von-Laue-Straße 1, 60438 Frankfurt am Main, Germany

[7]*Institut für Theoretische Physik und Astrophysik, Julius-Maximilians-Universität Würzburg, Am Hubland, D-97074 Würzburg, Germany*

[8]*Institut für Physik, Otto-von-Guericke-Universität Magdeburg, P.O. Box 4120, 39016 Magdeburg, Germany*

[9]*Max-Planck-Institut für Physik Komplexer Systeme, Nöthnitzer Straße 38, D-01187 Dresden, Germany*

[10]*Research Institute for Interdisciplinary Science, Okayama University, Okayama 700-8530, Japan*
(Dated: December 21, 2023)

The square-kagome lattice Heisenberg antiferromagnet is a highly frustrated Hamiltonian whose material realizations have been scarce. We theoretically investigate the recently synthesized $Na_6Cu_7BiO_4(PO_4)_4Cl_3$ where a Cu^{2+} spin-$1/2$ square-kagome lattice (with six site unit cell) is decorated by a seventh magnetic site alternatingly above and below the layers. The material does not show any sign of long-range magnetic order down to 50 mK despite a Curie-Weiss temperature of -212 K indicating a quantum paramagnetic phase. Our DFT energy mapping elicits a purely antiferromagnetic Hamiltonian that features longer range exchange interactions beyond the pure square-kagome model and, importantly, we find the seventh site to be strongly coupled to the plane. We combine two variational Monte Carlo approaches, pseudo-fermion/Majorana functional renormalization group and Schwinger-Boson mean field calculations to show that the complex Hamiltonian of $Na_6Cu_7BiO_4(PO_4)_4Cl_3$ still features a nonmagnetic ground state. We explain how the seventh Cu^{2+} site actually aids the stabilization of the disordered state. We predict static and dynamic spin structure factors to guide future neutron scattering experiments.

Introduction. Magnetic ions forming the kagome lattice, a corner sharing network of triangles, have been the focus of several decades of highly frustrated magnetism research [1]. Kagome lattice antiferromagnets provide some of the most promising examples of highly correlated nonmagnetic ground states [2, 3], and are therefore subject of intense experimental efforts while inspiring a wealth of theoretical developments [4, 5]. Interestingly, the square-kagome lattice as a differently connected lattice of corner sharing triangles [6], can also support a quantum paramagnetic ground state [7–12]. The precise nature of the ground state is under debate, with proposals spanning a pinwheel valence bond crystal (VBC) [13, 14], length six loop VBC [15, 16], and (lattice) nematic quantum spin liquid [17]. The field of frustrated quantum magnetism is currently poised with the arrival of new materials based on the square-kagome lattice geometry promising to host exotic nonmagnetic phases at low temperatures [18–21]. In the most prominently studied example $KCu_6AlBiO_4(SO_4)_5Cl$, the Cu^{2+} $S = 1/2$ moments do not show any sign of long-range dipolar magnetic order down to 50 mK despite Curie-Weiss temperatures of -237 K, with indications of gapless quantum spin liquid behavior [22]. Recently, $Na_6Cu_7BiO_4(PO_4)_4[Cl,(OH)]_3$, a novel sodium bismuth oxo-cuprate phosphate chloride containing square-kagome layers of Cu^{2+} ions was synthesized [18]. It contains, besides the six magnetic sites making up the square-kagome lattice, a seventh decorating site which is placed either above or below the square in checkerboard fashion. A study of specific heat indicates that the compound does not order magnetically down to 50 mK [19] despite a large negative Curie-Weiss temperature of -212 K. The scenario in both these compounds is then strikingly similar to the kagome lattice based candidate quantum spin liquid material Herbertsmithite [1].

In this work, we will establish the Hamiltonian of $Na_6Cu_7BiO_4(PO_4)_4Cl_3$ by density functional theory based energy mapping. As it is highly nontrivial to work out the ground state and excited state properties of this complex lattice with three symmetry inequivalent magnetic sites, we apply two types of variational Monte Carlo (VMC), two flavors of functional renormalization group (FRG) calculations and the Schwinger boson (SB) formalism. We establish that the Hamiltonian of $Na_6Cu_7BiO_4(PO_4)_4Cl_3$ indeed realizes a nonmagnetic ground state, and provide evidence that the seventh magnetic site decorating the square-kagome lattice plays an important role in enhancing the degree of frustration, thus aiding the formation of a magnetically disordered phase in this material. This phase is shown to be a gapped VBC breaking translation symmetry, with a dimer pattern that is periodic in a 2×2 enlarged unit cell. We present its spectroscopic signatures to compare with future neutron scattering experiments.

Heisenberg Hamiltonian. We determined the magnetic interactions of $Na_6Cu_7BiO_4(PO_4)_4Cl_3$ using all electron density functional theory calculations. We use the crystal structure
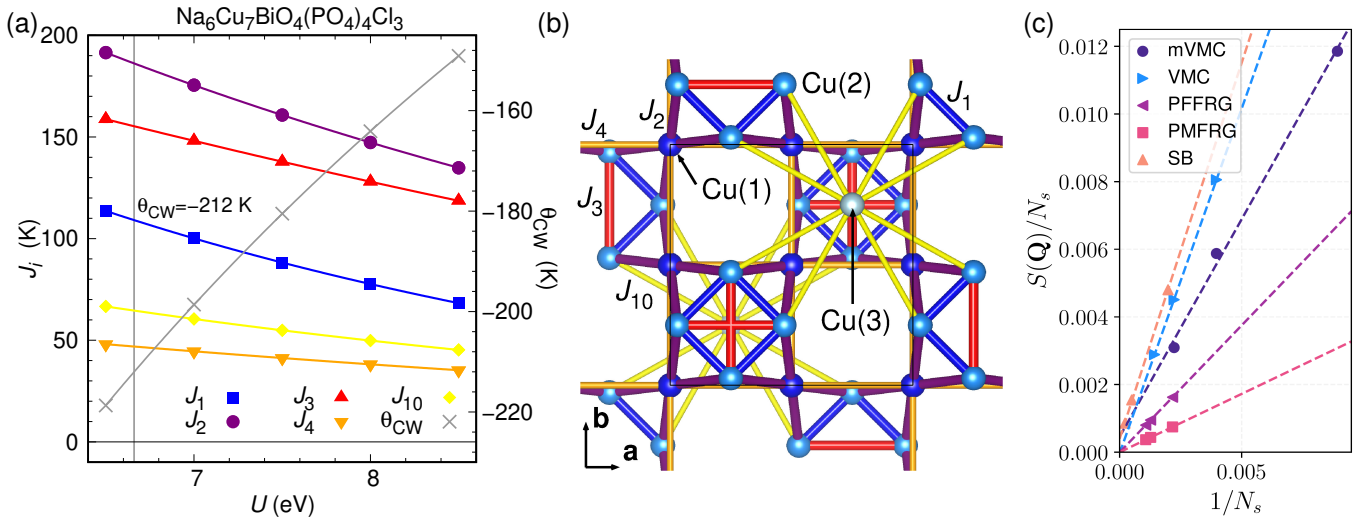
FIG. 1. (a) Heisenberg Hamiltonian parameters of $Na_6Cu_7BiO_4(PO_4)_4Cl_3$ determined by DFT energy mapping as function of onsite interaction strength U (negligible couplings are not shown). The vertical line indicates the U value where the exchange couplings match the experimental [18] Curie-Weiss temperature. The resulting nonnegligible exchange couplings are $J_1 = 109.1(8)$ K, $J_2 = 186.2(7)$ K, $J_3 = 155.3(1.4)$ K, $J_4 = 46.9(4)$ K, $J_{10} = 64.6(2)$ K. (b) Relevant exchange paths of $Na_6Cu_7BiO_4(PO_4)_4Cl_3$. (c) Finite-size scaling of the maxima of the equal-time structure factor $S(\mathbf{Q})/N_s$ from many-variable VMC (mVMC), VMC, pseudo-fermion FRG (PFFRG), pseudo-Majorana FRG (PMFRG) (at $T = 0.2J_2$), and the Schwinger-Boson mean-field theory method. Note that, compared to the other methods, PFFRG and PMFRG use a different definition of the system size N_s, which counts the number of correlated sites around a reference site, likely explaining the quantitative differences of our results. Furthermore, PMFRG results are obtained at a finite temperature $T = 0.2J_2$.

determined in Ref. 18 but simplify it slightly by choosing the majority Na(2) position and by removing O(5) from the Cl(3) position. All 14 Cu^{2+} ions in the primitive unit cell of the tetragonal structure are in square planar coordination with oxygen. The network they form is shown in Fig. 1 (b), with the three symmetry inequivalent Cu(1), Cu(2) and Cu(3) shown in different colors. Cu(1) and Cu(2) form a square-kagome lattice, and Cu(3) is decorating this lattice above and below. Spin-polarized calculations show that the Cu^{2+} ions have $S = \frac{1}{2}$ moments, and at $U = 6.5$ eV the system is insulating with a gap of $E_g = 1.7$ eV. We use the energy mapping technique that has yielded very good results in other copper based magnets [23, 24] to extract the Heisenberg Hamiltonian parameters. Figure 1 (a) shows the result of these calculations. Exchange couplings evolve smoothly with the on-site Coulomb repulsion U, and the Hamiltonian reproduces the experimental Curie-Weiss temperature at $U = 6.66$ eV (vertical line). Some couplings that are less than 3% of the largest coupling J_2 are not shown in the plot. Among the couplings we resolve, there is only one, negligibly small, interlayer coupling (see Ref. [25]); as there is a full Na and Cl layer separating the magnetic layers, we expect the deviations from magnetic two-dimensionality to be small and beyond the scope of the present study. The two couplings making up the square-kagome lattice, $J_1 = 0.59J_2$ and J_2, are the third largest and largest coupling, respectively. The diagonal in the squares, $J_3 = 0.83J_2$, is the second largest coupling. One second nearest neighbor of the square-kagome lattice, $J_4 = 0.25J_2$, is also substantial. Furthermore, the $J_{10} = 0.35J_2$ interaction, which couples the square-kagome site Cu(2) to the magnetic

decorating sites Cu(3) is found to be important. Strong buckling of the square-kagome lattice means that this coupling is the closest connection between Cu(3) and Cu(2) sites. It has a reasonable superexchange path through a phosphate group. On the other hand, the closer connection of a Cu(3) site to a Cu(1) site turns out to be negligible ($J_5 = 0.03J_2$).

The space group $P4/nmm$ of $Na_6Cu_7BiO_4(PO_4)_4Cl_3$ dictates that the J_1 (light blue) square and the J_2 (purple) triangle couplings are symmetry inequivalent as for the ideal lattice. The isotropic $J_1 = J_2$ Heisenberg antiferromagnet is host to a VBC ground state with a finite spin gap $\Delta \sim 0.04J_1$ [15], whose precise nature is still under debate [13–16]. For $J_2/J_1 \geqslant 2$, classically the system is host to a long-range ferrimagnetically ordered ground state (up-up-down) [10], however, for $S = 1/2$, exact diagonalization studies on $N = 24, 30, 36$ site clusters [10, 26, 27] find that the system enters the ferrimagnetic ground state for $J_2/J_1 \gtrsim 1.65$. The DFT estimated material couplings with $J_2/J_1 \sim 1.7$ thus precariously places the system in the vicinity of the nonmagnetic-magnetic phase boundary. It is then likely that the significant J_3 diagonal couplings ($J_3/J_1 \sim 1.45$) within the squares generate the necessary frustration to tip the balance in favor of a nonmagnetic ground state. If so, the precise nature of the nonmagnetic state, in the presence of further neighbor coupling J_4 and the coupling J_{10} to the decorating Cu(3) site, needs to be carefully investigated by probing the delicate energetic competition between various quantum spin liquid and VBC ansätze.

Results. We begin our analysis by addressing the issue of the existence of long-range magnetic order in the ground state of
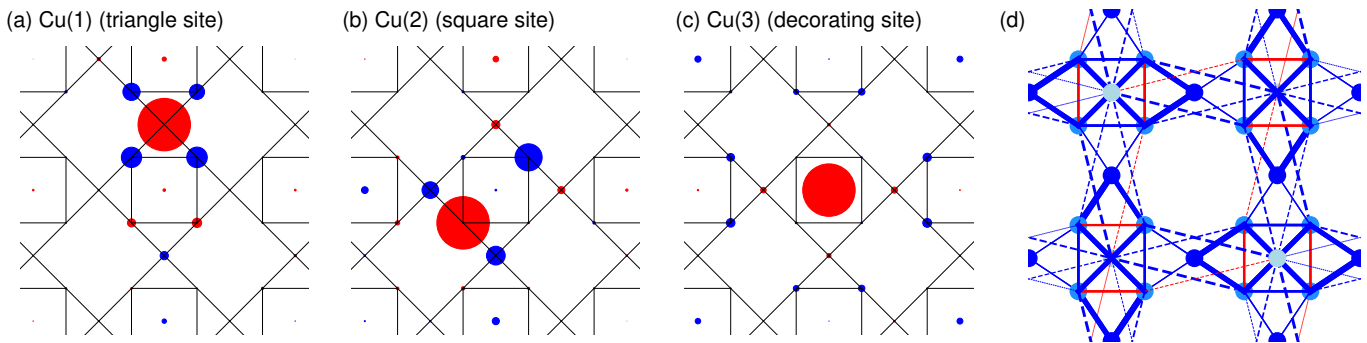
FIG. 2. (a)-(c) The pattern of real space (equal-time) spin-spin correlations $\langle \hat{\mathbf{S}}_i \cdot \hat{\mathbf{S}}_j \rangle$ from mVMC measured with respect to the three symmetry inequivalent sites. The radius of the circle is proportional to the magnitude of the correlator and blue (red) denote antiferromagnetic (ferromagnetic) correlations. The largest red circle corresponds to $i = j$. (d) The pattern of $\langle \hat{\mathbf{S}}_i \cdot \hat{\mathbf{S}}_j \rangle$ within a 2×2 unit cell showing the pattern of strong/weak bonds in the VBC ground state. The thickness is proportional to $|\langle \hat{\mathbf{S}}_i \cdot \hat{\mathbf{S}}_j \rangle|$ and blue (red) denote antiferromagnetic (ferromagnetic) bonds, while the dashed lines denote the J_{10} bonds. Note that the idealized 2D unit cell shown here is rotated by $45°$ with respect to Fig. 1(b).

the DFT Hamiltonian. Employing state-of-the-art numerical approaches of mVMC [28, 29], fermionic VMC [30, 31], PF-FRG [32–34], PMFRG [35, 36], and SB analysis [17, 37–40], we compute the static (equal-time) spin structure factor

$$S(\mathbf{q}) = \frac{1}{N_s} \sum_{0 \leqslant i, j < N_s} \langle \hat{\mathbf{S}}_i \cdot \hat{\mathbf{S}}_j \rangle e^{i\mathbf{q}\cdot(\mathbf{r}_i - \mathbf{r}_j)}, \qquad (1)$$

where N_s is the number of sites in the lattice, $\mathbf{q}$ is a momentum inside the extended Brillouin zone, and $\mathbf{r}_i$ denotes the site positions (accounting for sublattice displacements), following the convention outlined in Supp. Mat. [25]. Long-range dipolar magnetic order sets in when the maximum of $S(\mathbf{q})$ at $\mathbf{q} = \mathbf{Q}$ scales as $S(\mathbf{Q}) \propto N_s$ for large N_s [41]. The size scaling of $S(\mathbf{Q})/N_s$ [see Fig. 1 (c)], yields the magnetization $m^2 \propto \lim_{N_s \to \infty} S(\mathbf{Q})/N_s$, which we consistently find to be zero (within error bars) from different approaches. This provides evidence for a nonmagnetic ground state which is corroborated by the rapid decay of the real space spin-spin correlations seen in Fig. 2 (a)–(c) [see Ref. 25 for results from fermionic VMC and Schwinger boson approaches].

To further elucidate the nature of the nonmagnetic ground state, we perform mVMC simulations with *ansätze* of different unit cell sizes. Table I shows variational ground state energies for the $Na_6Cu_7BiO_4(PO_4)_4Cl_3$ Hamiltonian on three different clusters after symmetrization. The energies without the J_{10} coupling to Cu(3) sites are also given. Independent of the system size, the energies for 2×2 enlarged, i.e.,

Unit cell	4×4	6×6	8×8	
1×1	-0.4256(1)	-0.4205(1)	-0.4172(1)	⎫ With Cu(3)
2×2	-0.4426(1)	-0.4304(1)	-0.4277(1)	⎭
1×1	-0.4729(1)	-0.4783(1)	-0.4698(2)	⎫ Without
2×2	-0.4857(1)	-0.4816(1)	-0.4811(2)	⎭ Cu(3)

TABLE I. mVMC energies E/J_2 on the 4×4, 6×6 and 8×8 lattices with a 1×1 and 2×2 unit cell after symmetrization.

24-site unit cells are slightly (about 2%) lower compared to translation invariant states, i.e., either quantum spin liquids or lattice nematic. Other independent approaches reach similar conclusions, lending support for a translation symmetry broken ground state. These include a fermionic VMC analysis guided by different ansätze, a self-consistent fermionic mean-field analysis of different U(1) and $\mathbb{Z}_2$ spin liquids [42], as well as a Schwinger-Boson mean-field study. The pattern of real space (equal-time) spin-spin correlations is shown in Fig. 2(d), which points to its VBC nature. Here, one observes a checkerboard pattern, whereby the J_1 bonds featuring ferromagnetic (antiferromagnetic) correlations are always complemented by J_2 bonds hosting strong (weak) antiferromagnetic correlations thus forming a staggered horizontal/vertical pattern. The frustrating diagonal bonds inside the squares (J_3) show the strongest (antiferromagnetic) correlations, while the Cu(2) and Cu(3) sites are also found to be strongly correlated via J_{10} bonds, the latter highlighting the decorated nature of the lattice geometry. The VBC pattern possesses only C_2 symmetry.

Interestingly, we notice that the inclusion of J_{10} interactions in the Hamiltonian increases the frustration thereby enhancing the disordering tendency. This is reflected in an increase of the ground state energy per site [see Table I] and decreasing correlations between Cu(1) and Cu(2) sites in favor of bonds containing a Cu(3) site (see Fig. S7 in Ref. 25). In particular, the ratio of $J_{10}/J_2 \sim 0.34$ places the material in the vicinity of the high point of frustration (largest ground state energy) (Table S2 in Ref. 25). In mVMC calculations, the effect of increasing J_{10} is to induce the rotation and reflection symmetry breaking, and broadening of the maxima in S($\mathbf{q}$) leading to a more diffuse signal (see Fig. S4 in Ref. 25). Thus, an important aspect of this result is that despite an appreciable magnetic coupling of the decorated Cu(3) ions with the square-kagome layers, it does not result in magnetic ordering. Quite the contrary, we show that the presence of these strongly correlated interlayer Cu^{2+} ions aids the stabilization of a mag-

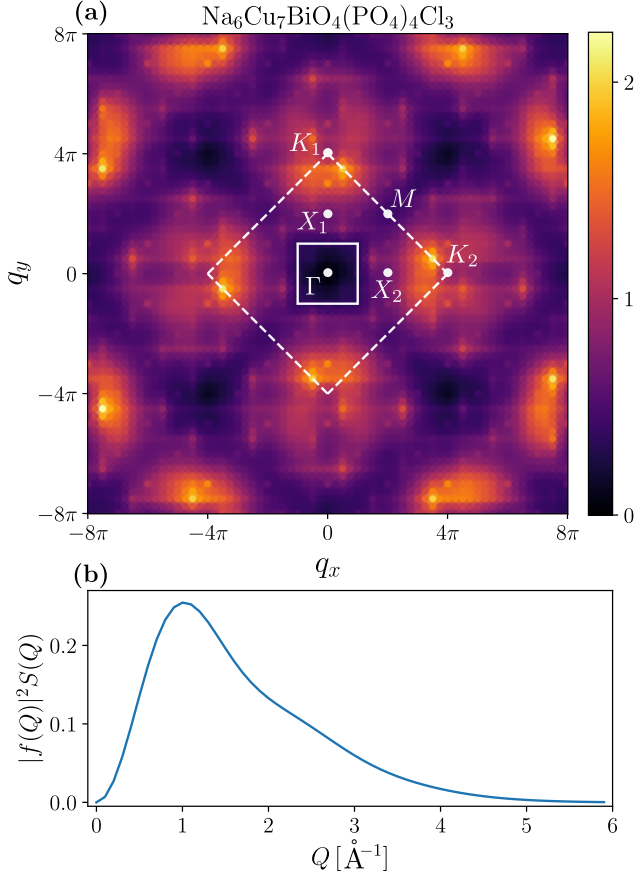FIG. 3. (a) Static (equal-time) structure factor from mVMC [Eq. (1)] obtained w.r.t. true crystal lattice site positions [25] obtained on a $8\times8\times7$ site cluster [Note: the $(S\mathbf{q})$ is not periodic, and the Brillouin zones and high-symmetry points of the ideal geometrical lattice are only drawn for illustrative purposes], (b) The corresponding powder average after accounting for the form factor.

netically disordered ground state – thus settling the question raised by specific heat measurements [19]. It is interesting to note that in a related square-kagome material nabokoite $KCu_7TeO_4(SO_4)_5Cl$ which similarly features decorating Cu sites, signatures of long-range ordering have recently been reported [20].

The symmetry breaking manifests itself in the static spin structure factor which is likewise C_2 symmetric [see Fig. 3(a)] as obtained from mVMC. The maxima are located at $\mathbf{q} = \pm2\pi(3.75, 2.25)$ with the follow-up maxima at $\mathbf{q} = \pm2\pi(1.75, 0.25)$. The powder average structure factor is presented in Fig. 3(b) in order to facilitate comparison with potential neutron scattering studies.

The flexibility of the SBMFT method allows to efficiently compute the dynamical structure factor

$$S(\mathbf{q},\omega) = \frac{1}{N_s}\sum_{i,j} e^{i\mathbf{q}\cdot(\mathbf{r_i}-\mathbf{r_j})}\int_{-\infty}^{\infty} dt e^{-i\omega t}\langle\hat{\mathbf{S}}_i(t)\hat{\mathbf{S}}_j(0)\rangle,$$
(2)

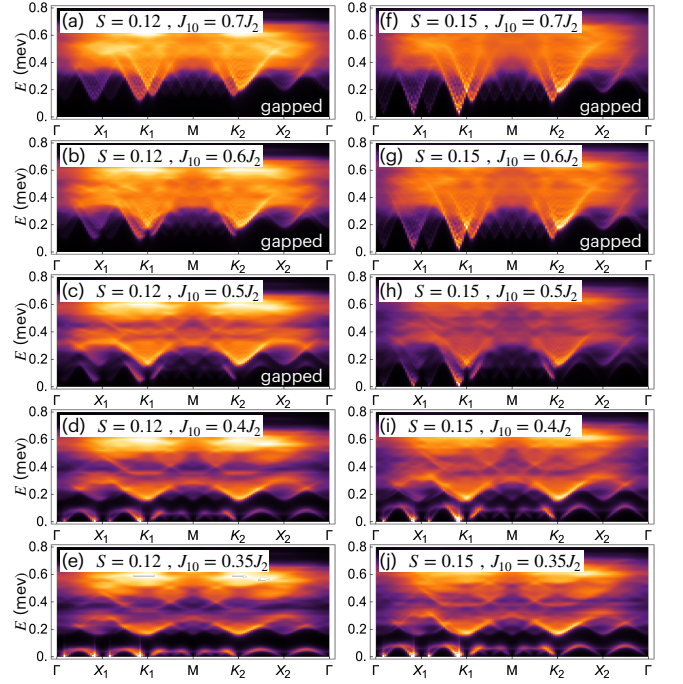and to extract interesting magnon features with information

FIG. 4. Dynamical structure factors as function of S and J_{10}. The other parameters are as given in the caption of Fig 1. As J_{10} increases and/or S decreases, a gap opens and a quantum paramagnet is stabilized. The Bose condensations appear at incommensurate q vectors. In the condensed state, the Cu(3) spins are ordered but the other spins in the square-kagome lattice remain very weakly ordered. This is reflected by the gap between the lower branch excitations and the continuum in the lower panels.

on the Bose condensations of specific branches. Here, N_s is the total number of sites given by $n_u \times 2 \times l \times l$, where n_u is the number of sites per unit cell (here 14 in the presence of the Cu(3) atoms), and l is the linear size of the system. This quantity can be compared with with neutron scattering experiments. Within this approach one can artificially tune S to lower values in order to enhance quantum fluctuations [40, 43]. Thus, in Fig. 4, we show the dynamical structure factor for two representative spin values $S = 0.12, 0.15$ for which a quantum paramagnetic ground state can be stabilized, and also for various values of Cu(3) coupling, J_{10}, for a system size of $l = 12$ with 4032 spins. This figure displays several features: (i) decreasing J_{10} or increasing S favours Bose condensation of the Cu(3) atom spins, (ii) they appear at incommensurate values of the BZ, (iii) the rotational symmetry breaking is evident from asymmetric excitation spectra around the K_1 and K_2 points, see Fig. 3(a) and (iv) the gap closes at the extracted parameters but a secondary gap between the lower branch and the continuum appears, reflecting ordered Cu(3) spins, while the others remain weakly ordered. This allows us to reveal the proximity to a phase transition between a quantum paramagnetic state and its Bose condensate counterpart.

As seen in the fermion approaches, the effect of projecting the wave function on exact physical states increases the quantum

fluctuations and help the system to remain disordered even in the presence of the Cu(3) atoms. In the SBMFT, since magnetic orders are more competitive by construction, they are favoured at $S = 1/2$. Thus, in order to reach the quantum paramagnet, one has to reduce the spin value.

We can see that the Bose condensation arises on the Cu(3) spins while the others on the square-kagome lattice remain disordered. This is reflected in Fig. 4 in a clear gap in the lower panels between the condensed branches and the excitations in the continuum [see Fig. S11 of Supp. Mat. [25] for real space spin correlation profiles]. As one can see, a clear magnetic order appears on the Cu(3) spins while the spins on the square-kagome lattice are disordered.

Conclusions We have determined a Heisenberg Hamiltonian for $Na_6Cu_7BiO_4(PO_4)_4Cl_3$ with five significant antiferromagnetic exchange interactions. While triangle couplings in the square-kagome lattice dominate at about twice the size of the square couplings, the diagonals in the squares are the second largest interaction. The Cu(3) sites decorating the square kagome lattice in $Na_6Cu_7BiO_4(PO_4)_4Cl_3$ turn out to be substantially coupled to the square sites. Our five numerical techiques all corroborate that the Hamiltonian has a nonmagnetic ground state, in agreement with the fact that experimentally, no order was found down to 50 mK. We find the nature of this ground state to be a VBC which breaks translational symmetry. We predict static as well as dynamical structure factors to motivate studies of $Na_6Cu_7BiO_4(PO_4)_4Cl_3$ with inelastic neutron scattering.

----

* These authors contributed equally.

[1] M. R. Norman, Colloquium: Herbertsmithite and the search for the quantum spin liquid, Rev. Mod. Phys. **88**, 041002 (2016).

[2] Y. Iqbal, F. Becca, S. Sorella, and D. Poilblanc, Gapless spin-liquid phase in the kagome spin-$\frac{1}{2}$ Heisenberg antiferromagnet, Phys. Rev. B **87**, 060405(R) (2013).

[3] Y.-C. He, M. P. Zaletel, M. Oshikawa, and F. Pollmann, Signatures of Dirac cones in a DMRG study of the kagome Heisenberg model, Phys. Rev. X **7**, 031020 (2017).

[4] A. Harrison, First catch your hare*: the design and synthesis of frustrated magnets, J. Phys.: Condens. Matter **16**, S553 (2004).

[5] L. Savary and L. Balents, Quantum spin liquids: a review, Rep. Prog. Phys. **80**, 016502 (2016).

[6] R. Siddharthan and A. Georges, Square kagome quantum antiferromagnet and the eight-vertex model, Phys. Rev. B **65**, 014417 (2001).

[7] J. Richter, J. Schulenburg, P. Tomczak, and D. Schmalfuß, The Heisenberg antiferromagnet on the square-kagomé lattice, Condens. Matter Phys. **12**, 507 (2009).

[8] H. Nakano and T. Sakai, The Two-Dimensional S=1/2 Heisenberg Antiferromagnet on the Shuriken Lattice –A Lattice Composed of Vertex-Sharing Triangles–, J. Phys. Soc. Jpn. **82**, 083709 (2013).

[9] Y. Hasegawa, H. Nakano, and T. Sakai, Metamagnetic jump in the spin-$\frac{1}{2}$ antiferromagnetic Heisenberg model on the square kagome lattice, Phys. Rev. B **98**, 014404 (2018).

[10] K. Morita and T. Tohyama, Magnetic Phase Diagrams and Magnetization Plateaus of the Spin-1/2 Antiferromagnetic Heisenberg Model on a Square-Kagome Lattice with Three Nonequivalent Exchange Interactions, J. Phys. Soc. Jpn. **87**, 043704 (2018).

[11] P. Tomczak and J. Richter, Specific heat of the spin-1/2 Heisenberg antiferromagnet on squagome lattice, J. Phys. A **36**, 5399 (2003).

[12] M. Gembé, H.-J. Schmidt, C. Hickey, J. Richter, Y. Iqbal, and S. Trebst, Noncoplanar magnetic order in classical square-kagome antiferromagnets, Phys. Rev. Res. **5**, 043204 (2023).

[13] N. Astrakhantsev, F. Ferrari, N. Niggemann, T. Müller, A. Chauhan, A. Kshetrimayum, P. Ghosh, N. Regnault, R. Thomale, J. Reuther, T. Neupert, and Y. Iqbal, Pinwheel valence bond crystal ground state of the spin-$\frac{1}{2}$ Heisenberg antiferromagnet on the shuriken lattice, Phys. Rev. B **104**, L220408 (2021).

[14] I. Rousochatzakis, R. Moessner, and J. van den Brink, Frustrated magnetism and resonating valence bond physics in two-dimensional kagome-like magnets, Phys. Rev. B **88**, 195109 (2013).

[15] P. Schmoll, A. Kshetrimayum, J. Naumann, J. Eisert, and Y. Iqbal, Tensor network study of the spin-$\frac{1}{2}$ Heisenberg antiferromagnet on the shuriken lattice, Phys. Rev. B **107**, 064406 (2023).

[16] A. Ralko and I. Rousochatzakis, Resonating-Valence-Bond Physics Is Not Always Governed by the Shortest Tunneling Loops, Phys. Rev. Lett. **115**, 167202 (2015).

[17] T. Lugan, L. D. C. Jaubert, and A. Ralko, Topological nematic spin liquid on the square kagome lattice, Phys. Rev. Res. **1**, 033147 (2019).

[18] O. V. Yakubovich, L. V. Shvanskaya, G. V. Kiriukhina, A. S. Volkov, O. V. Dimitrova, and A. N. Vasiliev, Hydrothermal Synthesis and a Composite Crystal Structure of $Na_6Cu_7BiO_4(PO_4)_4[Cl,(OH)]_3$ as a Candidate for Quantum Spin Liquid, Inorg. Chem. **60**, 11450 (2021).

[19] B. Liu, Z. Zeng, A. Xu, Y. Sun, O. Yakubovich, L. Shvanskaya, S. Li, and A. Vasiliev, Low-temperature specific-heat studies on two square-kagome antiferromagnets, Phys. Rev. B **105**, 155153 (2022).

[20] M. M. Markina, P. S. Berdonosov, T. M. Vasilchikova, K. V. Zakharov, A. F. Murtazoev, V. A. Dolgikh, A. V. Moskin, V. N. Glazkov, A. I. Smirnov, and A. N. Vasiliev, Static and resonant properties of decorated square kagome lattice compound $KCu_7(TeO_4)(SO_4)_5Cl$ (2022), arXiv:2212.11623 [cond-mat.str-el].

[21] A. F. Murtazoev, K. A. Lyssenko, M. M. Markina, V. A. Dolgikh, A. N. Vasiliev, and P. S. Berdonosov, New Nabokoite-like Phases $ACu_7TeO_4(SO_4)_5Cl$ (A=Na, K, Rb, Cs) with Decorated and Distorted Square Kagome Lattices, Chem. Phys. Chem. **24**, e202300111 (2023).

[22] M. Fujihala, K. Morita, R. Mole, S. Mitsuda, T. Tohyama, S.-i. Yano, D. Yu, S. Sota, T. Kuwai, A. Koda, H. Okabe, H. Lee, S. Itoh, T. Hawai, T. Masuda, H. Sagayama, A. Matsuo, K. Kindo, S. Ohira-Kawamura, and K. Nakajima, Gapless spin liquid in a square-kagome lattice antiferromagnet, Nat. Commun. **11**, 3429 (2020).

[23] H. O. Jeschke, F. Salvat-Pujol, E. Gati, N. H. Hoang, B. Wolf, M. Lang, J. A. Schlueter, and R. Valentí, Barlowite as a canted antiferromagnet: Theory and experiment, Phys. Rev. B **92**, 094417 (2015).

[24] M. Hering, F. Ferrari, A. Razpopov, I. I. Mazin, R. Valentí, H. O. Jeschke, and J. Reuther, Phase diagram of a distorted kagome antiferromagnet and application to Y-kapellasite, npj Comput. Mater. **8**, 10 (2022).

[25] See Supplemental Material at [TO BE INSERTED BY THE EDITORS] for additional information on and results from DFT energy mapping, multivariable variational Monte Carlo and variational Monte Carlo methods, pseudo-Fermion and pseudo-Majorana functional renormalization group approaches and Schwinger boson method. (See also references [17, 18, 28–31, 35–40, 44–49] therein).

[26] J. Richter and J. Schnack, Magnetism of the $S = \frac{1}{2}$ $J_1 - J_2$ square-kagome lattice antiferromagnet, Phys. Rev. B **107**, 245115 (2023).

[27] J. Richter, O. Derzhko, and J. Schnack, Thermodynamics of the spin-half square kagome lattice antiferromagnet, Phys. Rev. B **105**, 144427 (2022).

[28] T. Misawa, S. Morita, K. Yoshimi, M. Kawamura, Y. Motoyama, K. Ido, T. Ohgoe, M. Imada, and T. Kato,

mVMC—Open-source software for many-variable variational Monte Carlo method, Comput. Phys. Commun **235**, 447 (2019).

[29] D. Tahara and M. Imada, Variational Monte Carlo Method Combined with Quantum-Number Projection and Multi-Variable Optimization, J. Phys. Soc. Jpn. **77**, 114701 (2008).

[30] S. Sorella, Green Function Monte Carlo with Stochastic Reconfiguration, Phys. Rev. Lett. **80**, 4558 (1998).

[31] F. Becca and S. Sorella, *Quantum Monte Carlo Approaches for Correlated Systems* (Cambridge University Press, Cambridge, United Kingdom, 2017).

[32] J. Reuther and P. Wölfle, $J_1 - J_2$ frustrated two-dimensional Heisenberg model: Random phase approximation and functional renormalization group, Phys. Rev. B **81**, 144410 (2010).

[33] Y. Iqbal, R. Thomale, F. Parisen Toldin, S. Rachel, and J. Reuther, Functional renormalization group for three-dimensional quantum magnetism, Phys. Rev. B **94**, 140408(R) (2016).

[34] T. Müller, D. Kiese, N. Niggemann, B. Sbierski, J. Reuther, S. Trebst, R. Thomale, and Y. Iqbal, Pseudo-fermion functional renormalization group for spin models (2023), arXiv:2307.10359 [cond-mat.str-el].

[35] N. Niggemann, B. Sbierski, and J. Reuther, Frustrated quantum spins at finite temperature: Pseudo-Majorana functional renormalization group approach, Phys. Rev. B **103**, 104431 (2021).

[36] N. Niggemann, J. Reuther, and B. Sbierski, Quantitative functional renormalization for three-dimensional quantum Heisenberg models, SciPost Phys. **12**, 156 (2022).

[37] A. Auerbach, *Interacting electrons and quantum magnetism* (Springer Science & Business Media, 1998).

[38] J. C. Halimeh and M. Punk, Spin structure factors of chiral quantum spin liquids on the kagome lattice, Phys. Rev. B **94**, 104413 (2016).

[39] R. Schaffer, Y. Huh, K. Hwang, and Y. B. Kim, Quantum spin liquid in a breathing kagome lattice, Phys. Rev. B **95**, 054410 (2017).

[40] T. Lugan, L. D. C. Jaubert, M. Udagawa, and A. Ralko, Schwinger boson theory of the $J_1, J_2 = J_3$ kagome antiferromagnet, Phys. Rev. B **106**, L140404 (2022).

[41] A. W. Sandvik, Finite-size scaling of the ground-state parameters of the two-dimensional Heisenberg model, Phys. Rev. B **56**, 11678 (1997).

[42] Atanu Maity and Yasir Iqbal, In preparation.

[43] L. Messio, B. Bernu, and C. Lhuillier, Kagome Antiferromagnet: A Chiral Topological Spin Liquid?, Phys. Rev. Lett. **108**, 207204 (2012).

[44] K. Koepernik and H. Eschrig, Full-potential nonorthogonal local-orbital minimum-basis band-structure scheme, Phys. Rev. B **59**, 1743 (1999).

[45] J. P. Perdew, K. Burke, and M. Ernzerhof, Generalized gradient approximation made simple, Phys. Rev. Lett. **77**, 3865 (1996).

[46] A. I. Liechtenstein, V. I. Anisimov, and J. Zaanen, Density-functional theory and strong interactions: Orbital ordering in Mott-Hubbard insulators, Phys. Rev. B **52**, R5467 (1995).

[47] K. Momma and F. Izumi, *VESTA3* for three-dimensional visualization of crystal, volumetric and morphology data, J. Appl. Crystallogr. **44**, 1272 (2011).

[48] P. Ghosh, T. Müller, Y. Iqbal, R. Thomale, and H. O. Jeschke, Effective spin-1 breathing kagome Hamiltonian induced by the exchange hierarchy in the maple leaf mineral bluebellite, arXiv (2023), arXiv:2301.05224 [cond-mat.str-el].

[49] G. Carleo and M. Troyer, Solving the quantum many-body problem with artificial neural networks, Science **355**, 602 (2017).

Quantum paramagnetism in the decorated square-kagome antiferromagnet $Na_6Cu_7BiO_4(PO_4)_4Cl_3$
– Supplemental Material –

Nils Niggemann,[1,2,3,*] Nikita Astrakhantsev,[4,*] Arnaud Ralko,[5,3,*] Francesco Ferrari,[6,3,*] Atanu Maity,[3] Tobias Müller,[7] Johannes Richter,[8,9] Ronny Thomale,[7,3] Titus Neupert,[4] Johannes Reuther,[1,2,3] Yasir Iqbal,[3] and Harald O. Jeschke[10,3]

[1]*Dahlem Center for Complex Quantum Systems and Fachbereich Physik, Freie Universität Berlin, 14195 Berlin, Germany*
[2]*Helmholtz-Zentrum für Materialien und Energie, Hahn-Meitner-Platz 1, 14109 Berlin, Germany*
[3]*Department of Physics and Quantum Centre of Excellence for Diamond and Emergent Materials (QuCenDiEM),*
Indian Institute of Technology Madras, Chennai 600036, India
[4]*Department of Physics, University of Zürich, Winterthurerstrasse 190, CH-8057 Zürich, Switzerland*
[5]*Institut Néel, UPR2940, Université Grenoble Alpes, CNRS, Grenoble, FR-38042 France*
[6]*Institut für Theoretische Physik, Goethe Universität Frankfurt,*
Max-von-Laue-Straße 1, 60438 Frankfurt am Main, Germany
[7]*Institut für Theoretische Physik und Astrophysik, Julius-Maximilians-Universität Würzburg, Am Hubland, D-97074 Würzburg, Germany*
[8]*Institut für Physik, Otto-von-Guericke-Universität Magdeburg, P.O. Box 4120, 39016 Magdeburg, Germany*
[9]*Max-Planck-Institut für Physik Komplexer Systeme, Nöthnitzer Straße 38, D-01187 Dresden, Germany*
[10]*Research Institute for Interdisciplinary Science, Okayama University, Okayama 700-8530, Japan*
(Dated: December 21, 2023)

ADDITIONAL DFT INFORMATION

Density functional theory calculations were performed with the full potential local orbital (FPLO) basis [S2] and a generalized gradient approximation (GGA) exchange correlation functional [S3]. Strong electronic correlations on Cu $3d$ orbitals are taken into account by a DFT+U method [S4]. We show the full result of the energy mapping procedure for $Na_6Cu_7BiO_4(PO_4)_4Cl_3$ in Table S1. For every considered value of the onsite interaction strength U, a total of 68 energies were calculated with $4{\times}4{\times}4$ **k**-point meshes. The line in bold face is interpolated to yield the experimental Curie-Weiss temperature $\theta_{CW} = -212$ K [S1]. As discussed in the main text, only five of the thirteen determined exchange interactions are substantial and are considered in the many-body calculations for $Na_6Cu_7BiO_4(PO_4)_4Cl_3$. The only interlayer coupling J_{15} we determined is small enough that $Na_6Cu_7BiO_4(PO_4)_4Cl_3$
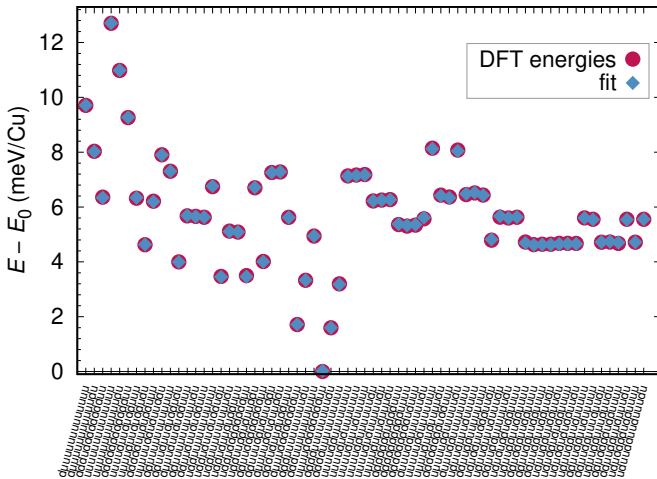

FIG. S1. Quality of energy mapping in $Na_6Cu_7BiO_4(PO_4)_4Cl_3$. 68 calculated DFT energies are very precisely matched by the Heisenberg Hamiltonian with 13 exchange interactions.

can be treated as a 2D system.

In Fig. S1, we show that the energy mapping approach works very well for $Na_6Cu_7BiO_4(PO_4)_4Cl_3$. In $P1$ symmetry, all 14 Cu^{2+} moments can be set independently, and for the 68 chosen spin configurations, the comparison between DFT energy and fit to the Heisenberg Hamiltonian is excellent.

LATTICE CONVENTION

Each layer of the compound $Na_6Cu_7BiO_4(PO_4)_4Cl_3$ is represented by a square-kagome lattice with an additional site at the center of each shuriken (square surrounded by four triangles). More precisely, we define the unit vectors

$$\mathbf{a}_1 = (1,0), \quad \mathbf{a}_2 = (0,1), \tag{S1}$$

and a unit cell consisting of seven sites, labelled from A to G as shown in Fig. S2, whose relative coordinates are

$$\boldsymbol{\delta}_A = (0, 1/2), \ \boldsymbol{\delta}_B = (1/4, 3/4)$$
$$\boldsymbol{\delta}_C = (1/4, 1/4), \ \boldsymbol{\delta}_D = (3/4, 1/4)$$
$$\boldsymbol{\delta}_E = (3/4, 3/4), \ \boldsymbol{\delta}_F = (1/2, 1)$$
$$\boldsymbol{\delta}_G = (2/4, 2/4) \tag{S2}$$

In this convention, all sites lie at rational fractions of the basis vectors, which ensures a finite extended Brillouin zone over which the structure factor is periodic. The lattice for this compound features three types of symmetry inequivalent sites, namely those that lie on the vertices of each shuriken (A, F), the corners of each square (B, C, D, E) and the center sites G [see Fig. S2]. Although, the geometry of the lattice does not alter the physics (once the couplings are fixed), for comparison with experiments, it is required to compute Fourier-transformed quantities with respect to the lattice of the original compound. As most numerical methods do not explicitly employ real-space crystallographic coordinates but

U (eV)	J_1 (K)	J_2 (K)	J_3 (K)	J_4 (K)	J_5 (K)	J_6 (K)	J_8 (K)	J_9 (K)	J_{10} (K)	J_{13} (K)	J_{14} (K)	J_{15} (K)	J_{20} (K)	θ_{CW} (K)
6.5	113.6(8)	191.5(7)	158.7(1.4)	48.1(4)	5.8(4)	0.6(4)	-0.8(7)	3.4(8)	66.6(2)	-2.2(6)	2.0(4)	0.3(4)	-0.1(4)	-218.7
6.66	**109.1(8)**	**186.2(7)**	**155.3(1.4)**	**46.9(4)**	**5.3(4)**	**0.6(4)**	**-1.1(7)**	**3.2(8)**	**64.6(2)**	**-2.2(6)**	**1.9(4)**	**0.3(4)**	**0.0(4)**	**-212**
7	100.1(7)	175.5(6)	148.1(1.1)	44.6(4)	4.4(4)	0.5(3)	-1.5(5)	2.9(7)	60.5(2)	-2.1(5)	1.8(3)	0.2(4)	0.0(3)	-198.6
7.5	88.2(6)	160.8(5)	137.8(9)	41.3(3)	3.2(3)	0.5(3)	-1.9(4)	2.6(6)	54.9(2)	-2.1(4)	1.6(3)	0.2(3)	0.0(2)	-180.5
8	77.7(5)	147.3(4)	128.0(7)	38.2(2)	2.3(3)	0.4(2)	-2.2(4)	2.2(5)	49.8(1)	-2.0(3)	1.5(2)	0.2(2)	0.0(2)	-164.1
8.5	68.3(4)	134.8(3)	118.6(6)	35.3(2)	1.6(2)	0.4(2)	-2.4(3)	2.0(4)	45.3(1)	-1.8(3)	1.4(2)	0.1(2)	0.0(2)	-149.1
d (Å)	3.11405	3.27801	4.40394	5.0088	5.26566	5.33981	5.72746	5.76923	6.01815	6.55602	7.08351	7.71676	8.22822	

TABLE S1. Exchange interactions of $Na_6Cu_7BiO_4(PO_4)_4Cl_3$ obtained by DFT energy mapping as described in the main text. The line in bold face corresponds to the set of couplings that match the experimental Curie-Weiss temperature [S1].
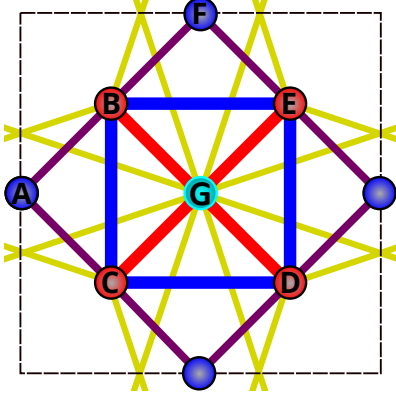

FIG. S2. Idealized square-kagome unit cell. Sites A and F correspond to Cu(1) ions, sites B, C, D, E to Cu(2) ions and site G to the Cu(3) ion in the unit cell of $Na_6Cu_7BiO_4(PO_4)_4Cl_3$.
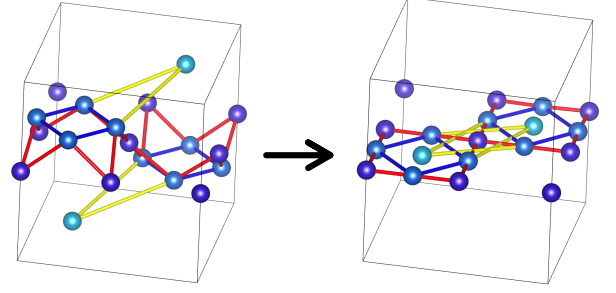

FIG. S3. Mapping from 3D lattice to 2D lattice. To compute Eq. (S3), sites are mapped to the idealized lattice convention. Visualization done using VESTA [S5].

rather the more abstract graph of sites and respective bonds, this amounts to a choice in the post-processing of real-space data. In the following, we outline this step in detail. We define the Fourier transform of the spin susceptibility as

$$\chi(\mathbf{q}) = \frac{1}{N}\sum_{i,j}\chi(\mathbf{r}_i, \mathbf{r}_j)e^{i\mathbf{q}\cdot(\mathbf{r}_i-\mathbf{r}_j)}. \qquad (S3)$$

Here, the vectors $\mathbf{q}, \mathbf{r}_i$ are three-dimensional, accounting for the true crystallographic coordinates, and allowing for distortions outside of the square-kagome planes which occur in the crystal structure. We must therefore map each pair of sites of the true 3D lattice to a unique site in the idealized lattice.

Upon noting that the layers are decoupled (as we neglect the tiny J_{15} exchange interaction) and correlations between two sites from different layers are zero, we can immediately interpret the summation to go over sites in a single layer only.

The mapping we need to perform can then be written as $f(n_1, n_2, 0, n_b) = (n_1', n_2', n_b')$, where we define $\mathbf{r}_i = n_1\mathbf{a}_1 + n_2\mathbf{a}_2 + \mathbf{b}_{n_b}$. Since the unit cell of the three-dimensional lattice can be enlarged compared to the idealized one, it may be cumbersome to find this mapping directly. A convenient strategy is to work in Cartesian coordinates, mapping $\mathbf{r}_i$ to a $2D$ point (x, y) which lies on the idealized lattice. Then, the Cartesian coordinates (x, y) can be transformed back into either a lattice position (n_1, n_2, n_b), or a site index i. This is shown in Fig. S3.

To compare with powder samples, we compute the powder averaged structure factor

$$S(Q) \equiv \frac{1}{4\pi}\int d\Omega\, S(\mathbf{q}), \quad Q = |\mathbf{q}| \qquad (S4)$$

and multiply by the form factor to account for nuclear scattering on Cu^{2+} ions [S6]

$$f(Q) = Ae^{-a\frac{Q^2}{4\pi}} + Be^{-b\frac{Q^2}{4\pi}} + C_1 e^{-c\frac{Q^2}{4\pi}} + D_1 \qquad (S5)$$
$$A = 0.0232,\ B = 0.4023$$
$$C_1 = 0.5882,\ D_1 = -0.0137$$
$$a = 34.969,\ b = 11.564,\ c = 3.843.$$

METHODS

Many-variable variational Monte Carlo (mVMC)

In this work, we employ the many-variable variational Monte Carlo implementation presented in Refs. [S7, S8]. To apply mVMC, spin operators are first mapped to pseudo-fermionic bilinears through the Abrikosov representation

$$\hat{\mathbf{S}}_i = \frac{1}{2}\sum_{\alpha,\beta=\downarrow,\uparrow}\hat{c}_{i,\alpha}^\dagger \boldsymbol{\sigma}_{\alpha,\beta}\hat{c}_{i,\beta}. \qquad (S6)$$

Inspired by Anderson's resonating valence-bond wave function, the mVMC ansatz has the form

$$|\phi_{\mathrm{pair}}\rangle = \hat{\mathcal{P}}_{\mathrm{G}}^{\infty}\exp\left(\sum_{i,j}f_{i,j}\hat{c}_{i,\uparrow}^\dagger \hat{c}_{j,\downarrow}^\dagger\right)|0\rangle, \qquad (S7)$$
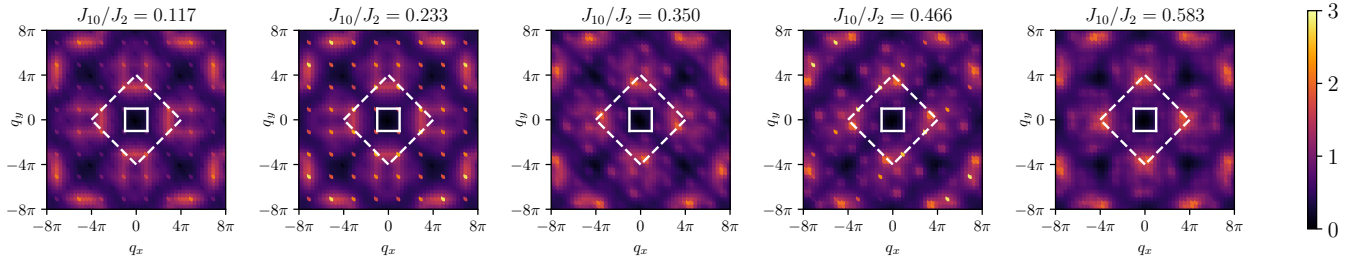
FIG. S4. Momentum-resolved equal-time spin structure factor calculated from mVMC on the $6 \times 6 \times 6$ lattice for different values of J_{10}/J_2. The Fourier transform is performed with respect to the ideal lattice coordinates of Eq. (S2). The wave functions were obtained with the symmetrization technique, enforcing the trivial representation. The solid and dashed lines denote the first and the extended Brillouin zones, respectively. The corresponding energies of these wave functions are given in Table S2.

where a fermionic wave function is constrained to a space of singly occupied sites by means of the Gutzwiller projector $\hat{\mathcal{P}}_{\mathrm{G}}^{\infty} = \prod_i (n_{i,\uparrow} - n_{i,\downarrow})^2$, where $n_{i,\sigma} = \hat{c}_{i,\sigma}^{\dagger} \hat{c}_{i,\sigma}$. The wave-function value $\langle \boldsymbol{\sigma} | \phi_{\mathrm{pair}} \rangle$ for a specific spin configuration $|\boldsymbol{\sigma}\rangle$ is evaluated using the Slater determinant of the matrix with elements $f_{i,j}$. The parameters $f_{i,j}$ are optimized using the stochastic reconfiguration optimization technique [S9–S11]. We may force a wave function to transform as a specific irreducible representation of the symmetry group. To this end, we apply its generators until the symmetry orbit is exhausted

$$|\Psi_{\xi}\rangle = \hat{P}|\Psi\rangle = \sum_n \xi^n \hat{G}^n |\Psi\rangle, \qquad (S8)$$

where ξ is the desired projection quantum number and $|\Psi_{\xi}\rangle$ the resulting symmetrized state. In the mVMC package, the projection onto the total spin S is performed by superposing the $SU(2)$–rotated wave functions [S8].

In Fig. S4, we show the equal-time spin structure factor for different values of J_{10}/J_2 measured within mVMC on the 6×6 lattice. The corresponding wave function energies are given in Table S2. One may see that the frustration grows until $J_{10}/J_2 \approx 0.3$, which is manifested by growing energy and progressively diffuse character of the structure factor, and then rapidly decays with further increase in J_{10}/J_2.

Variational Monte Carlo (VMC)

Analogously to mVMC, the fermionic variational Monte Carlo calculations of this work make use of a Gutzwiller-projected wave function to approximate the ground state of the spin Hamiltonian by minimization of the variational energy. The VMC trial state reads

$$|\Psi_0\rangle = \hat{\mathcal{J}} \hat{\mathcal{P}}_{\mathrm{G}}^{\infty} |\Phi_0\rangle, \qquad (S9)$$

where $\hat{\mathcal{P}}_{\mathrm{G}}^{\infty}$ is the Gutzwiller projector, $|\Phi_0\rangle$ is a fermionic Slater determinant [in the Abrikosov fermion representation of spins Eq. (S6)] and $\hat{\mathcal{J}}$ is a spin-spin Jastrow factor. The definition of the fermionic state $|\Phi_0\rangle$ is done by the introduction of an auxiliary fermionic Hamiltonian

$$\hat{\mathcal{H}}_0 = \sum_{i,j,\alpha} \chi_{ij} \hat{c}_{i,\alpha}^{\dagger} \hat{c}_{j,\alpha}, \qquad (S10)$$

whose hopping amplitudes, χ_{ij}, play the role of variational parameters. The presence of the spin-spin Jastrow factor

$$\hat{\mathcal{J}} = \exp\left(\sum_{i,j} v_{i,j} \hat{S}_i^z \hat{S}_j^z\right) \qquad (S11)$$

can enhance/suppress spin-spin correlations between lattice sites. We consider a long-range Jastrow factor with pseudopotential parameters that depend on the distance between sites, i.e., $v_{i,j} = v(\|\mathbf{r}_i - \mathbf{r}_j\|)$. The variational parameters defining $|\Psi_0\rangle$ are optimized by means of the stochastic reconfiguration method [S9, S10]. The VMC calculations are performed on finite-size lattices with periodic boundary conditions. Specifically, we employ two kinds of fully-symmetric clusters, one defined by the translation vectors $\mathbf{T}_1 = L\mathbf{a}_1$ and $\mathbf{T}_2 = L\mathbf{a}_2$ (containing $N_s = 7L^2$ sites), and the other defined by the vectors $\mathbf{T}_1 = L(\mathbf{a}_1 + \mathbf{a}_2)$ and $\mathbf{T}_2 = L(\mathbf{a}_1 - \mathbf{a}_2)$ (containing $N_s = 14L^2$ sites). The biggest lattice employed in our VMC calculations contains $N_s = 700$ spins.

The best variational energy is obtained by a parametrization of the auxiliary Hamiltonian in which the translational symmetry is broken. In particular, in agreement with mVMC observations, the optimal hopping pattern requires a doubling of the unit cell along $\mathbf{a}_1$ and $\mathbf{a}_2$ (2×2 periodicity). Concerning point group symmetries, the VMC wave function turns out to preserve the C_4 rotational symmetry around the center of the 2×2 supercell. The small C_4 to C_2 symmetry breaking found by mVMC calculations is not captured by the VMC variational ansatz. The spin structure factor $S(\mathbf{q})$ corresponding to the best variational state for the Heisenberg Hamiltonian of $Na_6Cu_7BiO_4(PO_4)_4Cl_3$ is shown in Fig. S5. The absolute maxima of $S(\mathbf{q})$ are located at $\mathbf{q} = (7\pi/2, \pi/2)$ and $\mathbf{q} = (\pi/2, 7\pi/2)$ (and symmetry related points). Compared
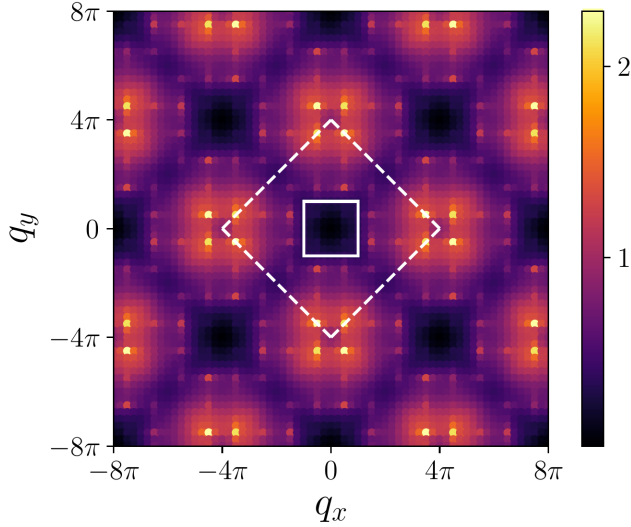
J_{10}/J_2	0.0	0.117	0.223	0.350	0.466	0.583
E/J_2	-0.4128	-0.4128	-0.4080	-0.4305	-0.4436	-0.4687

TABLE S2. Ground state energy E/J_2 per site obtained on the 6×6 lattice within mVMC for different ratios of J_{10}/J_2. The statistical error is kept around $\delta E/J_2 = 10^{-4}$.

FIG. S5. Equal-time spin structure factor $S(\mathbf{q})$ from VMC for the Hamiltonian of $Na_6Cu_7BiO_4(PO_4)_4Cl_3$. The results are obtained on a cluster with $N_s = 448$ sites, defined by the translation vectors $\mathbf{T}_1 = 8\mathbf{a}_1$ and $\mathbf{T}_2 = 8\mathbf{a}_2$, and plotted within the reciprocal space of the idealized lattice. The solid and dashed lines denote the first and the extended Brillouin zones, respectively.

to mVMC results, we find a larger intensity of the peaks of the structure factor, which can be ascribed to the presence of the Jastrow factor that enhances antiferromagnetic correlations.

PMFRG

The PMFRG formalism expresses spin operators by three different flavors (x, y, z) of Majorana fermions

$$S_i^x = -i\eta_i^y\eta_i^z, \qquad S_i^y = -i\eta_i^z\eta_i^x, \qquad S_i^z = -i\eta_i^x\eta_i^y. \tag{S12}$$

This representation has the advantage that no unphysical states are introduced, allowing for quantitatively correct predictions at finite temperature [S12, S13]. One of the key advantages of PMFRG is its high momentum space resolution which allows for an easy detection of incommensurate order. The only restriction is a cut-off of all correlations beyond a numerically chosen maximum distance L. In a paramagnet, correlation lengths are typically small and effectively zero beyond a characteristic correlation length ξ, which makes this approximation virtually exact. When the correlation length diverges, for instance at the critical point of a phase transition, a finite-size scaling analysis may be performed to give accurate estimates of the critical temperature [S13].

Figure S6 shows the equal-time spin structure factor at low temperature, featuring soft maxima at wave-vectors $(q_x, q_y) \sim (3\pi, \pi/2)$. We find the position of these maxima to be temperature dependent. At high temperatures $T \gg J_2$, the maxima reside at $(4\pi, \pi)$ and symmetry related points, while the position of the peak shifts as temperature is low-
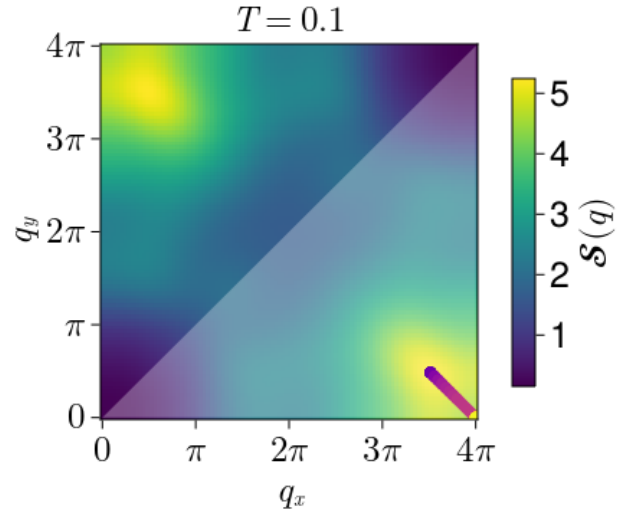

FIG. S6. Evolution of the maxima of the equal-time spin structure factor as a function of temperature obtained from PMFRG. The color of the line corresponds to the temperature, i.e., the yellow part corresponds to the highest simulated temperature ($T = 2.5J_2$, while the blue part indicates the lowest temperatures. The background shows the low temperature structure factor as a reference.

ered. In addition to the spin susceptibility χ defined in Eq. (S3), one may also define a sublattice-resolved susceptibility $\chi_{\alpha\beta}$, $\alpha, \beta = 1, 2, \ldots N_{UC}$, where $N_{UC} = 7$ such that $\chi(\mathbf{k}) = \frac{1}{N_{UC}}\sum_{\alpha\beta}\chi_{\alpha\beta}(\mathbf{k})$. To study the influence of the
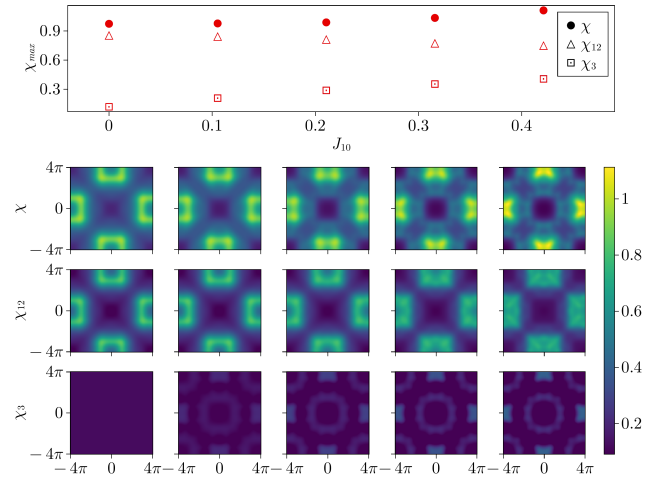

FIG. S7. From PMFRG, we show the evolution of the sublattice dependent susceptibilities defined in Eq. (S13) as a function of J_{10}. The top panel shows the respective maxima in momentum space, while the heat maps show the full momentum dependence. Note that points are shown for three different maximal correlation lengths of $L = 14, 16, 18$ nearest neighbor bonds, which all coincide, indicating absence of finite size effects.
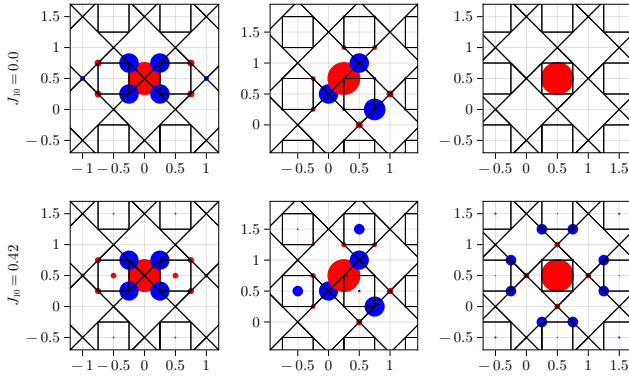
FIG. S8. Real space correlations $\langle \hat{\mathbf{S}}_i \cdot \hat{\mathbf{S}}_j \rangle$ computed from PMFRG by taking Cu(1) (left), Cu(2) (middle), and Cu(3) (right) as reference sites i. The radii of the circle indicates the strength of correlations, while the color red (blue) indicates a positive (negative) sign of the correlations.

Cu(3) sites, Fig. S7 further displays the susceptibilities

$$\chi_{12}(\mathbf{k}) \equiv \frac{1}{N_{\mathrm{UC}}} \sum_{\alpha\beta \neq Cu(3)} \chi_{\alpha\beta}(\mathbf{k})$$

$$\chi_3(\mathbf{k}) \equiv \chi(\mathbf{k}) - \chi_{12}(\mathbf{k}). \tag{S13}$$

Here, χ_{12} quantifies the correlations between all non-Cu(3) sites, and χ_3 the contribution to the susceptibility upon adding the Cu(3) site. The correlations between the Cu(1) and Cu(2) sites decrease upon strengthening the J_{10} bond while maxima of intensity become diffuse, indicating increased frustration. To see this, note that the conservation of spin magnitude dictates a sum rule within the extended BZ: $\sum_i \hat{\mathbf{S}}_i^2 = \sum_{\mathbf{q}} \langle \hat{\mathbf{S}}(-\mathbf{q})\hat{\mathbf{S}}(\mathbf{q}) \rangle = \mathrm{N}\frac{3}{4}$. As a consequence, the susceptibility $\chi_{\alpha\beta}(\mathbf{q})$ for non-interacting spins must be a non-zero constant (see, e.g., χ_3 in Fig. S7 at $J_{10} = 0$). Switching on the couplings between sites, leaves the sum rule intact for each sublattice but intensities may shift in reciprocal space and develop features. Therefore, the observed decrease in the maximum of χ_{12} indicates a more uniform distribution of different ordering wavevectors $\mathbf{q}$ within the system –a signature of the effects of frustration.

While the correlations between Cu(3) sites and the rest of the system naturally grow as they are increasingly coupled, ordering tendencies are absent as visible from the independence of our data on the maximal correlation length L above the accessible temperature range of $T \gtrsim 0.3 J_2$.

In Fig. S8, we also show the pattern of equal time spin-spin correlations in real space for the system with $J_{10} = 0$ and $J_{10} \approx 0.42 J_2$. It is visible that adding the additional Cu(3) site does not lead to increased correlations between the other sites and, in fact, slightly decreases them. Overall, we find good agreement to mVMC in Fig. 2 of the main text.

For comparison with experimental data, we compute the spin structure factor with respect to the actual crystal lattice site coordinates, i.e., allowing for atoms to be positioned out-
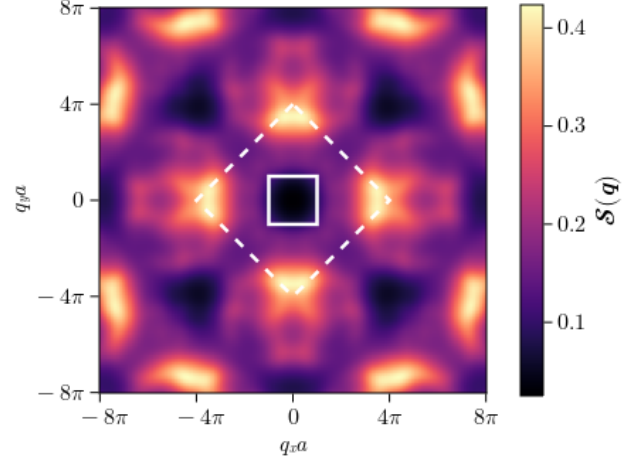

FIG. S9. Equal time structure factor $S(q, t = 0)$ at $T = 0.3 J_2$ for a cut at $q_z = 0$ computed with respect to the true, three dimensional crystallographic unit cell. Shown is the first BZ (solid), and the approximate extended BZ (dashed).
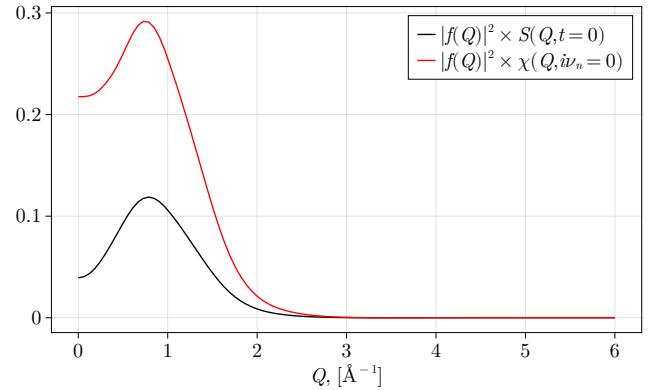

FIG. S10. Powder average of the equal time structure factor $S(Q, t = 0)$ and the static magnetic suscepibility $\chi(Q, i\nu_n = 0)$ at $T = 0.1 J_2$ obtainde from PMFRG. As in Fig. S9, the Fourier transform is performed with respect to the actual crystal lattice site coordinates.

side of a pure 2D layer. Figure S9 shows the corresponding momentum resolved equal-time spin structure factor projected onto the $q_x - q_y$ plane taking $q_z = 0$. We note that due to the irrational coordinates of the atoms within the unit cell, the structure factor is no longer periodic within any extended Brillouin zone. The structure factor permits points of high intensity away from $q_z = 0$, although they will naturally be broad, as length of correlations is limited in z direction due to the layered structure of the material. If we restrict ourselves to a finite box in momentum space between $|q_{x,y,z}| < 8\pi/a$, the maxima are positioned at incommensurate positions $\mathbf{k} = (0.61, 6.95, 0)\,\pi/a$. For experimental com-

parison, in Fig. S10, we further provide the powder averaged structure factor Eq. (S4).

SCHWINGER BOSON MEAN FIELD THEORY

As in the VMC section, it is possible to make a parton construction of the spin by introducing Schwinger bosons instead of Abrikosov fermions. We thus consider the decoupling:

$$\hat{\mathbf{S}}_i = \frac{1}{2} \sum_{\alpha,\beta=\downarrow,\uparrow} \hat{b}_{i,\alpha}^\dagger \boldsymbol{\sigma}_{\alpha,\beta} \hat{b}_{i,\beta}, \qquad (S14)$$

where $\hat{b}^{(+)}$ are now bosonic operators. The advantage of dealing with bosons as opposed to fermions is the possibility of having Bose condensation and thus to easily access quantum magnetic orders as well as $(\mathbb{Z}_2)$ quantum spin liquids, which are both treated on an equal footing. Here, we recall the main lines of the approach noting that more details can be found in [S14–S18]. In this approach, it is possible to write Heisenberg terms as function of two SU(2) invariant operators $\hat{A}$ and $\hat{B}$

$$\begin{aligned} \hat{A}_{ij} &= \frac{1}{2} \left[\hat{b}_{i\uparrow} \hat{b}_{j\downarrow} - \hat{b}_{i\downarrow} \hat{b}_{j\uparrow} \right] \\ \hat{B}_{ij} &= \frac{1}{2} \left[\hat{b}_{i\uparrow}^+ \hat{b}_{j\uparrow} + \hat{b}_{i\downarrow}^+ \hat{b}_{j\downarrow} \right] \end{aligned}$$

as

$$\hat{\mathbf{S}}_i \hat{\mathbf{S}}_j = : \hat{B}_{ij}^+ \hat{B}_{ij} : - \hat{A}_{ij}^+ \hat{A}_{ij}, \qquad (S15)$$

where :: denotes the normal ordering. At the mean field level, the Hamiltonian then reads

$$\begin{aligned} \mathcal{H}_{\text{SB}} &= = \sum_{i,j} J_{ij} \left[\hat{B}_{ij}^+ B_{ij} + \hat{B}_{ij} B_{ij}^* - \hat{A}_{ij}^+ A_{ij} - \hat{A}_{ij} A_{ij}^* \right] \\ &\quad - \sum_{i,j} J_{ij} \left[|B_{ij}|^2 - |A_{ij}|^2 \right] + \sum_i \lambda_i (\hat{n}_i - 2S), \quad (S16) \end{aligned}$$

with the mean field parameters $A_{ij} = \langle \phi_0 | \hat{A}_{ij} | \phi_0 \rangle$ and $B_{ij} = \langle \phi_0 | \hat{B}_{ij} | \phi_0 \rangle$ computed in $|\phi_0\rangle$ – the boson vacuum at $T = 0$ for each pair of interacting spins $(i \rightarrow j)$. Because the Hilbert space is enlarged by the mapping, it is necessary to fulfill the constraint $\hat{n}_i = \hat{b}_{i\uparrow}^+ \hat{b}_{i\uparrow} + \hat{b}_{i\downarrow}^+ \hat{b}_{i\downarrow} = 2S$ for a spin S. Thus, we have also introduced Lagrange multipliers λ_i to account for this on average. Another advantage of the method is that S can be treated as an external parameter and by reducing it, it is possible to enhance quantum fluctuations. This is particularly interesting if one wants to focus on phase transitions between a magnetically ordered state and its quantum spin liquid parent. Also, the flexibility of the method allows to compute the dynamical structure factor

$$S(\mathbf{q},\omega) = \frac{1}{n_s} \sum_{i,j} e^{i\mathbf{q}\cdot(\mathbf{r_i}-\mathbf{r_j})} \int_{-\infty}^{\infty} dt e^{-i\omega t} \langle \hat{\mathbf{S}}_i(t) \hat{\mathbf{S}}_j(0) \rangle, \qquad (S17)$$

and to extract relevant magnon features and study Bose condensations of specific branches. Here, n_s is the total number of sites given by $n_u \times 2 \times l \times l$, with n_u the number of sites per unit-cell (here 14 in the presence of the Cu(3) atoms), and l is the linear size of the system. This allows for comparison with neutron experiments.

In Fig. 4 of the main text, we show the dynamical structure factor for two representative spin values $S = 0.12, 0.15$ at which a quantum spin liquid (QSL) can be achieved, and for various values of Cu(3) coupling J_{10} for a system size of $l = 12$ with 4032 spins, showing the proximity of the phase transition between a quantum spin liquid state and its Bose condensate counterpart.

As seen in the fermion approaches, the effect of projecting the wave function onto exact physical states increases the quantum fluctuations and helps the system to remain disordered even in the presence of the Cu(3) atoms. In the Schwinger boson mean field theory, since magnetic orders are more competitive by construction, they are favoured at $S = 1/2$. Thus, in order to reach the QSL, one has to reduce the spin value. In Fig. 4 of the main text, we can see that the Bose condensation arises on the Cu(3) spins while the others on the square-kagome lattice remains mainly disordered. This is reflected by a clear gap in the lower panels between the condensed branches and the excitations in the continuum. To have a better view of this feature, we have plotted in Fig. S11 the real-space (equal-time) spin-spin correlations using three different reference sites on a Cu(3) spin (top panel), on a corner of a triangle (middle panel) and on a corner of a square plaquette (bottom panel).

As one can see, a clear magnetic order appears on the Cu(3) spins while the ones on the remaining square-kagome lattice are disordered. This last feature is in good agreement with the observations of increased correlations between the Cu(3) sites in PMFRG, although no order could be detected in the accessible temperature regime.

---

* These authors contributed equally.

[S1] O. V. Yakubovich, L. V. Shvanskaya, G. V. Kiriukhina, A. S. Volkov, O. V. Dimitrova, and A. N. Vasiliev, Hydrothermal Synthesis and a Composite Crystal Structure of $Na_6Cu_7BiO_4(PO_4)_4[Cl,(OH)]_3$ as a Candidate for Quantum Spin Liquid, Inorg. Chem. **60**, 11450 (2021).

[S2] K. Koepernik and H. Eschrig, Full-potential nonorthogonal local-orbital minimum-basis band-structure scheme, Phys. Rev. B **59**, 1743 (1999).

[S3] J. P. Perdew, K. Burke, and M. Ernzerhof, Generalized gradient approximation made simple, Phys. Rev. Lett. **77**, 3865 (1996).

[S4] A. I. Liechtenstein, V. I. Anisimov, and J. Zaanen, Density-functional theory and strong interactions: Orbital ordering in Mott-Hubbard insulators, Phys. Rev. B **52**, R5467 (1995).

[S5] K. Momma and F. Izumi, *VESTA3* for three-dimensional visualization of crystal, volumetric and morphology data, J. Appl. Crystallogr. **44**, 1272 (2011).
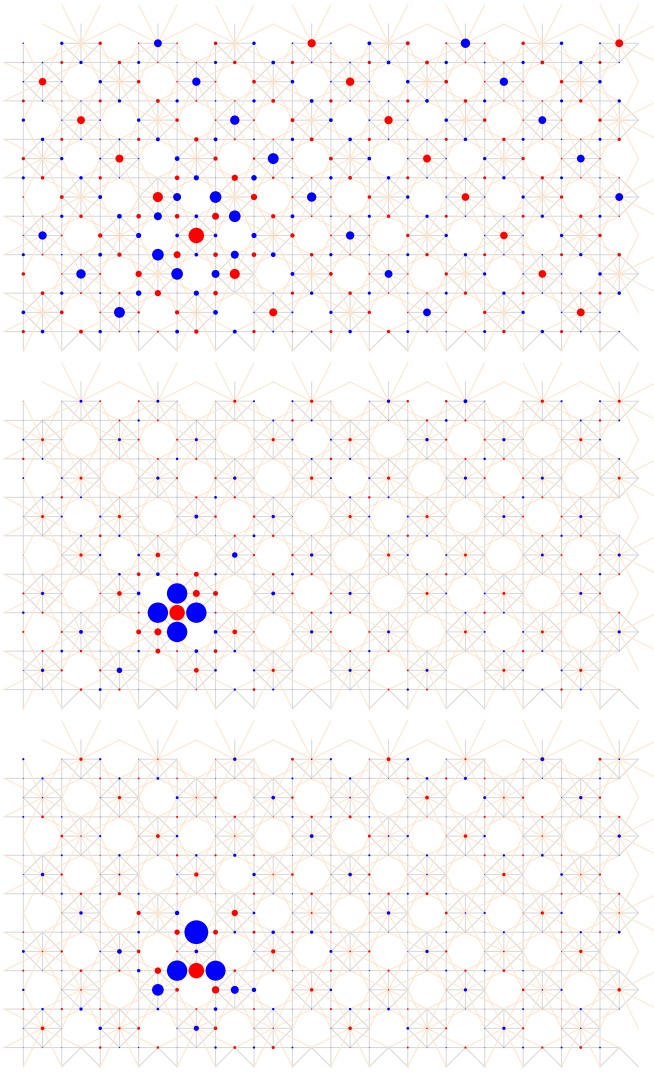
FIG. S11. Real space (equal-time) spin-spin correlations considering 3 reference sites: (top) Cu(3) spin, (middle) corner of triangles and (bottom) corner of square plaquette. The parameters are the ones extracted in the main text, $S \simeq 0.366$ here, for which the sum rule of the static structure factor is satisfied [S18]. The system size is $n_u \times 2 \times 6 \times 6$. The colors correspond to positive (blue) and negative (red) correlations. The reference site is always the largest red disk of the figure.

[S6] P. Ghosh, T. Müller, Y. Iqbal, R. Thomale, and H. O. Jeschke, Effective spin-1 breathing kagome Hamiltonian induced by the exchange hierarchy in the maple leaf mineral bluebellite, arXiv (2023), arXiv:2301.05224 [cond-mat.str-el].

[S7] T. Misawa, S. Morita, K. Yoshimi, M. Kawamura, Y. Motoyama, K. Ido, T. Ohgoe, M. Imada, and T. Kato, mVMC—Open-source software for many-variable variational Monte Carlo method, Comput. Phys. Commun 235, 447 (2019).

[S8] D. Tahara and M. Imada, Variational Monte Carlo Method Combined with Quantum-Number Projection and Multi-Variable Optimization, J. Phys. Soc. Jpn. 77, 114701 (2008).

[S9] S. Sorella, Green Function Monte Carlo with Stochastic Reconfiguration, Phys. Rev. Lett. 80, 4558 (1998).

[S10] F. Becca and S. Sorella, *Quantum Monte Carlo Approaches for Correlated Systems* (Cambridge University Press, Cambridge, United Kingdom, 2017).

[S11] G. Carleo and M. Troyer, Solving the quantum many-body problem with artificial neural networks, Science 355, 602 (2017).

[S12] N. Niggemann, B. Sbierski, and J. Reuther, Frustrated quantum spins at finite temperature: Pseudo-Majorana functional renormalization group approach, Phys. Rev. B 103, 104431 (2021).

[S13] N. Niggemann, J. Reuther, and B. Sbierski, Quantitative functional renormalization for three-dimensional quantum Heisenberg models, SciPost Phys. 12, 156 (2022).

[S14] A. Auerbach, *Interacting electrons and quantum magnetism* (Springer Science & Business Media, 1998).

[S15] J. C. Halimeh and M. Punk, Spin structure factors of chiral quantum spin liquids on the kagome lattice, Phys. Rev. B 94, 104413 (2016).

[S16] R. Schaffer, Y. Huh, K. Hwang, and Y. B. Kim, Quantum spin liquid in a breathing kagome lattice, Phys. Rev. B 95, 054410 (2017).

[S17] T. Lugan, L. D. C. Jaubert, and A. Ralko, Topological nematic spin liquid on the square kagome lattice, Phys. Rev. Res. 1, 033147 (2019).

[S18] T. Lugan, L. D. C. Jaubert, M. Udagawa, and A. Ralko, Schwinger boson theory of the $J_1, J_2 = J_3$ kagome antiferromagnet, Phys. Rev. B 106, L140404 (2022).